Research Article | Vol. 26, No. 1 | 8 Jan 2018 | OPTICS EXPRESS 1
Optics EXPRESS

Thermally sensitive scattering of terahertz waves by coated cylinders for tunable invisibility and masking

ANDRIY E. SEREBRYANNIKOV,[1,*] KAMIL B. ALICI,[2] EKMEL OZBAY,[3,4] AND AKHLESH LAKHTAKIA[5]

[1]*Faculty of Physics, Adam Mickiewicz University, 61-614 Poznań, Poland*
[2]*TUBITAK Space Technologies Research Institute, 06800 Ankara, Turkey*
[3]*NANOTAM–Nanotechnology Research Center, Bilkent University, 06800 Ankara, Turkey*
[4]*Department of Physics, Department of Electrical and Electronics Engineering, and UNAM–Institute of Materials Science and Nanotechnology, Bilkent University, 06800 Ankara, Turkey*
[5]*Pennsylvania State University, Department of Engineering Science and Mechanics, Nanoengineered Metamaterials Group, University Park, Pennsylvania 16802, USA*
[*]*andser@amu.edu.pl*

Abstract: Temperature-sensitive scattering of terahertz (THz) waves by infinitely long, cylindrical core-shell structures was theoretically studied. Each structure is a dielectric cylinder coated with an InSb shell illuminated by either a transverse-electric (TE) or a transverse-magnetic (TM) plane wave. InSb is a thermally tunable semiconductor showing a transition from dielectric to plasmonic state at THz frequencies. Accordingly, the total scattering efficiency (TSE) can be thermally tuned for both polarization states of the incident plane wave. The spectral locations of the maxima and minima of the TSE of an InSb-coated cylinder can be exploited for cloaking the core. At least three scenarios lead to the strong suppression of scattering by a single core-shell structure in different spectral regimes when the temperature is fixed. The excitation of localized surface-plasmon resonances is the feature being common for two of them, while the effect of volumetric resonance dominates in the third scenario. Regimes that are either highly or weakly sensitive to the core material were identified. Weak sensitivity enables masking, i.e., the core material cannot be identified by a far-zone observer. The TSE minima are usually significantly sensitive to the polarization state, but ones with weak sensitivity to the polarization state also exist.

OCIS codes: (290.5839) Scattering, invisibility; (160.6840) Thermo-optical materials; (240.6680) Surface plasmons.

References and links

1. D. Schurig, J. J. Mock, B. J. Justice, S. A. Cummer, J. B. Pendry, A. F. Starr, and D. R. Smith, "Metamaterial electromagnetic cloak at microwave frequencies," Science **314**(5801), 977–980 (2006).
2. N.-A. Nicorovici, G. W. Milton, R. C. McPhedran, and L. C. Botten, "Quasistatic cloaking of two-dimensional polarizable discrete systems by anomalous resonance," Opt. Express **15**(10), 6314–6323 (2007).
3. A. Alù and N. Engheta, "Plasmonic materials in transparency and cloaking problems: mechanism, robustness, and physical insights," Opt. Express **15**(6), 3318–3332 (2007).
4. A. E. Serebryannikov, P. V. Usik, and E. Ozbay, "Non-ideal cloaking based on Fabry-Perot resonances in single-layer high-index," Opt. Express **17**(19), 16869–16876 (2009).
5. G. Castaldi, I. Gallina, V. Galdi, A. Alù, and N. Engheta, "Power scattering and absorption mediated by cloak/anti-cloak interactions: a transformation-optics route toward invisible sensors," J. Opt. Soc. Am. B **27**(10), 2132–2140 (2010).
6. J. McPhillips, A. Murphy, M. P. Jonsson, W. R. Hendren, R. Atkinson, F. Höök, A. V. Zayats, and R. J. Pollard, "High-performance biosensing using arrays of plasmonic nanotubes," ACS Nano **4**(4), 2210–2216 (2010).
7. Z. Ruan and S. Fan, "Superscattering of light from subwavelength nanostructures," Phys. Rev. Lett. **105**(1), 013901 (2010).
8. G. X. Li, H. L. Tam, F. Y. Wang, and K. W. Cheah, "Half-cylindrical far field superlens with coupled Fabry–Perot cavities," J. Appl. Phys. **104**(9), 096103 (2008).
9. A. Salandrino and N. Engheta, "Far-field subdiffraction optical microscopy using metamaterial crystals: Theory and simulations," Phys. Rev. B **74**(7), 075103 (2006).
10. Q. Cheng, T. J. Cui, W. X. Jiang, and B. G. Cai, "An omnidirectional electromagnetic absorber made of metamaterials," New J. Phys. **12**(6), 063006 (2010).

#305840 https://doi.org/10.1364/OE.26.000001
Journal © 2018 Received 30 Aug 2017; revised 14 Oct 2017; accepted 1 Dec 2017; published 2 Jan 2018

Optics EXPRESS

11. H. Noh, Y. Chong, A. D. Stone, and H. Cao, "Perfect coupling of light to surface plasmons by coherent absorption," Phys. Rev. Lett. **108**(18), 186805 (2012).
12. S. A. Cummer, B.-I. Popa, D. Schurig, D. R. Smith, J. Pendry, M. Rahm, and A. Starr, "Scattering theory derivation of a 3D acoustic cloaking shell," Phys. Rev. Lett. **100**(2), 024301 (2008).
13. D. P. Gaillot, C. Croënne, and D. Lippens, "An all-dielectric route for terahertz cloaking," Opt. Express **16**(6), 3986–3992 (2008).
14. A. Alù and N. Engheta, "Effects of size and frequency dispersion in plasmonic cloaking," Phys. Rev. E. **78**(4), 045602 (2008).
15. P. Alitalo, F. Bongard, J.-F. Zurcher, J. Mosig, and S. Tretyakov, "Expermental verification of broadband cloaking using a volumetric cloak composed of periodically stacked cylindrical transmission-line networks," Appl. Phys. Lett. **94**(1), 014103 (2009).
16. A. E. Serebryannikov and E. Ozbay, "Non-ideal multifrequency cloaking using strongly dispersive materials," Physica B **405**(14), 2959–2963 (2010).
17. R. D. Averitt, S. L. Westcott, and N. J. Halas, "Linear optical properties of gold nanoshells," J. Opt. Soc. Am. B **16**(10), 1814–1823 (1999).
18. T. Christensen, A.-P. Jauho, M. Wubs, and N. A. Mortensen, "Localized plasmons in graphene-coated nanospheres," Phys. Rev. B **91**(12), 125414 (2015).
19. N.-A. P. Nicorovici, R. C. McPhedran, S. Enoch, and G. Tayeb, "Finite wavelength cloaking by plasmonic resonance," New J. Phys. **10**(11), 115020 (2008).
20. A. Mirzaei, I. V. Shadrivov, A. E. Miroshnichenko, and Y. S. Kivshar, "Cloaking and enhanced scattering of core-shell plasmonic nanowires," Opt. Express **21**(9), 10454–10459 (2013).
21. A. E. Miroshnichenko, "Off-resonance field enhancement by spherical nanoshells," Phys. Rev. A **81**(5), 053818 (2010).
22. I. Liberal, I. Ederra, R. Gonzalo, and R. W. Ziolkowski, "Superbackscattering from single dielectric particles," J. Opt. **17**(7), 072001 (2015).
23. Z. Ruan and S. Fan, "Design of subwavelength superscattering nanospheres," Appl. Phys. Lett. **98**(4), 043101 (2011).
24. A. V. Goncharenko, E. F. Venger, Y. C. Chang, and A. O. Pinchuk, "Arrays of core-shell nanospheres as 3D isotropic broadband ENZ and highly absorbing metamaterials," Opt. Mater. Express **4**(11), 2310–2322 (2014).
25. J. Ng, H. Chen, and C. T. Chan, "Metamaterial frequency-selective superabsorber," Opt. Lett. **34**(5), 644–646 (2009).
26. F. Morgan, J. McPhillips, G. Wurtz, S. A. Maier, A. V. Zayats, and R. Pollard, "Fabrication and optical properties of large-scale arrays of gold nanocavities based on rod-in-a-tube coaxials," Appl. Phys. Lett. **102**(10), 103103 (2013).
27. D. de Ceglia, S. Campione, M. A. Vincenti, F. Capolino, and M. Scalora, "Low-damping epsilon-near-zero slabs: Nonlinear and nonlocal optical properties," Phys. Rev. B **87**(15), 155140 (2013).
28. A. Alù and N. Engheta, "Multifrequency optical invisibility cloak with layered plasmonic shells," Phys. Rev. Lett. **100**(11), 113901 (2008).
29. C. A. Valagiannopoulos and P. Alitalo, "Electromagnetic cloaking of cylindrical objects by multilayer or uniform dielectric claddings," Phys. Rev. B **85**(15), 155402 (2012).
30. E. A. Velichko, "Evaluation of a graphene-covered dielectric microtube as a refractive-index sensor in the terahertz range," J. Opt. **18**(3), 035008 (2016).
31. P.-Y. Chen, J. Soric, Y. R. Padooru, H. M. Bernety, A. B. Yakovlev, and A. Alù, "Nanostructured graphene metasurface for tunable terahertz cloaking," New J. Phys. **15**(12), 123029 (2013).
32. M. Riso, M. Cuevas, and R. A. Depine, "Tunable plasmonic enhancement of light scattering and absorption in graphene coated subwavelength wires," J. Opt. **17**(7), 075001 (2015).
33. J. Zhu, J. Han, Z. Tian, J. Gu, Z. Chen, and W. Zhang, "Thermal broadband tunable terahertz metamaterials," Opt. Commun. **284**(12), 3129–3133 (2011).
34. J. Han, A. Lakhtakia, Z. Tian, X. Lu, and W. Zhang, "Magnetic and magnetothermal tunabilities of subwavelength-hole arrays in a semiconductor sheet," Opt. Lett. **34**(9), 1465–1467 (2009).
35. J. Han and A. Lakhtakia, "Semiconductor split-ring resonators for thermally tunable terahertz metamaterials," J. Mod. Opt. **56**(4), 554–557 (2009).
36. S. T. Bui, V. D. Hguyen, X. K. Bui, T. T. Nguyen, P. Lievens, Y. P. Lee, and D. L. Vu, "Thermally tunable magnetic metamaterials at THz frequencies," J. Opt. **15**(7), 075101 (2013).
37. C. Luo, D. Li, J. Yao, and F. Ling, "Direct thermal tuning of the terahertz plasmonic response of semiconductor metasurface," J. Electromagn. Waves Appl. **29**(18), 2512–2522 (2015).
38. M. Kim, J. Jeong, J. K. S. Poon, and G. V. Eleftheriades, "Vanadium-dioxide-assisted digital optical metasurfaces for dynamic wavefront engineering," J. Opt. Soc. Am. B **33**(5), 980–988 (2016).
39. T. G. Mackay and A. Lakhtakia, "Temperature-mediated transition from Dyakonov surface waves to surface-plasmon-polariton waves," IEEE Photonics J. **8**(5), 4202813 (2016).
40. F. Chiadini, V. Fiumara, T. G. Mackay, A. Scaglione, and A. Lakhtakia, "Temperature-mediated transition from Dyakonov-Tamm surface waves to surface-plasmon-polariton waves," J. Opt. **19**(8), 085002 (2017).
41. L. Kai and A. D'Alessio, "Finely stratified cylinder model for radially inhomogeneous cylinders normally irradiated by electromagnetic plane waves," Appl. Opt. **34**(24), 5520–5530 (1995).
42. I. Gurwich, N. Shiloah, and M. Kleiman, "The recursive algorithm for electromagnetic scattering by tilted infinite circular multilayered cylinder," J. Quant. Spectrosc. Radiat. Transf. **63**(2–6), 217–229 (1999).
43. S. Manickavasagam and M. P. Mengüç, "Scattering-matrix elements of coated infinite-length cylinders," Appl. Opt. **37**(12), 2473–2482 (1998).

Optics EXPRESS

44. G. Sinclair, "Theory of models of electromagnetic systems," Proc. IRE **36**(11), 1364–1370 (1948).
45. H. C. van de Hulst, *Light Scattering by Small Particles* (Dover Press, 1981).
46. R. W. Ziolkowski and A. D. Kipple, "Reciprocity between the effects of resonant scattering and enhanced radiated power by electrically small antennas in the presence of nested metamaterial shells," Phys. Rev. E. **72**(3), 036602 (2005).
47. H. R. Stuart and A. Pidwerbetsky, "Electrically small antenna elements using negative permittivity resonators," IEEE Trans. Antenn. Propag. **54**(6), 1644–1653 (2006).
48. E. Colak, A. E. Serebryannikov, P. V. Usik, and E. Ozbay, "Diffraction inspired unidirectional and bidirectional beam splitting in defect-containing photonic structures without interface corrugations," J. Appl. Phys. **119**(19), 193108 (2016).
49. M. Veysi, C. Guclu, O. Boyraz, and F. Capolino, "Thin anisotropic metasurfaces for simultaneous light focusing and polarization manipulation," J. Opt. Soc. Am. B **32**(2), 318–323 (2015).
50. A. E. Serebryannikov, E. Colak, T. Magath, and E. Ozbay, "Two types of single-beam deflection and asymmetric transmission in photonic structures without interface corrugations," J. Opt. Soc. Am. A **33**(12), 2450–2458 (2016).

1. Introduction

Scattering and absorption by core-shell cylinders and spheres have been a focus of optics research in the last two decades. A wide variety of cloaking [1–4], sensing [5,6], scattering enhancement [7], focusing [8], imaging [9], and absorption [10,11] scenarios have been demonstrated in different parts of electromagnetic spectrum with the use of these geometrically simple structures. The proposed approaches to invisibility and cloaking include those based on transformation optics [1,5,12,13], scattering cancellation (also known as plasmonic cloaking) [3,14], transmission lines [15], and Fabry–Perot resonances [4,16]. Localized-surface-plasmon resonances (LSPRs)—also called particle-plasmon resonances—have been extensively studied [17,18], being attractive for cloaking [2,19,20] and off-resonance field enhancement [21]. Scattering enhancement including superscattering [7,22,23] and absorption enhancement [5,10,11,24,25] also exemplify possible uses of core-shell structures. In addition to single core-shell scatterers, arrays of core-shell scatterers [6,24,26,27] and multilayered (half-)cylinders [8,9,28,29] have been studied. In particular, arrays of rod-in-a-tube coaxial structuress and arrays of plasmonic nanotubes have been proposed for sensing applications [24,26]. Moreover, the concept of invisible sensors has been suggested [5]. New opportunities in sensing are provided by the use of dynamically tunable components. For instance, LSPRs can be electrically tuned if the shell is a graphene monolayer [30]. The tunability of graphene components allow to significantly enhance or weaken scattering, thereby enabling electrically tunable cloaking [31] and electrical control of absorption [32].

Many materials change their response characteristics due to variation of magnetostatic field, temperature, and intensity of illuminating light. In particular, thermal tunability can be very efficient, if certain constitutive properties are strongly sensitive to temperature variations. Natural materials that fulfil this requirement include InSb, VO_2 and other vanadium oxides. Both InSb [33–37] and VO_2 [38] have been successfully used in tunable metamaterials and metasurfaces. Thermal tunability of electromagnetic surface-wave propagation has also been theoretically demonstrated [39,40].

In this paper, we study scattering of a linearly polarized plane wave by an infinitely long cylinder comprising a solid dielectric core with an InSb coating (shell). The wave vector of the incident plane wave is oriented normal to the axis of the cylinder. Either the plane wave is transverse-magnetically (TM) polarized (i.e., the magnetic field is oriented normally to the cylinder axis) or it is transvserse-electrically (TE) polarized (i.e., the electric field is oriented normally to the cylinder axis). InSb shows a transition from the dielectric state to the plasmonic state in the THz spectral regime as the temperature is increased [33–37,39,40].

Our main goal in this paper is to investigate thermally tunable scattering and, in particular, thermally tunable invisibility and masking. We identify which changes in the total scattering efficiency (TSE) are dynamically achievable by change of the absolute temperature from 295 K to 345 K and the sensitivity of those dynamic changes to the relative permittivity of the core. The changes refer to the spectral locations of the extrema of the TSE. Possible

Optics EXPRESS

exploitation in novel temperature sensors is beyond the scope of this paper. All results presented in this paper were obtained by using standard analytical treatments [41–43], which result from enforcing the continuity of tangential components of the electric and magnetic fields across the core/shell and shell/air interfaces. Despite the studied structures not being scalable [44] due to the specific temperature dependence of the relative permittivity of InSb, we present all results as functions of the normalized frequency ka ($k = 2\pi f/c$ is the free-space wavenumber, f is frequency, a is the outer radius of the shell, and c is the speed of light in free space) for convenience.

2. Geometry and material properties

Figure 1 presents the geometry of the boundary-value problem and the relative permittivity of InSb, the coating material. The infinitely long structure comprises (i) the cylindrical core of cross-sectional radius b and relative permittivity ε_c and (ii) the InSb shell with outer radius a, as shown in Fig. 1(a). The wave vector of the incident plane wave lies wholly in the xy plane, whereas the cylindrical axis is parallel to the z axis.

The main electromagnetic characteristic used in this paper is the total scattering efficiency

$$\sigma = (ka)^{-1} \sum_{n=-\infty}^{\infty} c_n^2 \tag{1}$$

where c_n stands for the amplitude of the nth-order partial wave in the scattered field. Equation (1) is a standard equation [45], in which each term in the sum over n corresponds to the order of cylindrical Bessel and Hankel functions used in the expansions of the field components in the core, shell, and the region beyond the shell [43]. A Matlab code was written based on analytical formulas and used to calculate the TSE and field distributions, after rigorous tests of convergence and accuracy.

In the THz regime, the relative permittivity of InSb obeys the Drude model [33,35]

$$\varepsilon_{\mathrm{InSb}}(\omega) = \varepsilon_\infty - \omega_p^2/(\omega^2 + i\gamma\omega) \tag{2}$$

where $\omega = 2\pi f$ is the angular frequency; $\varepsilon_\infty = 15.68$ is the high-frequency relative permittivity; $\gamma = 0.1\pi$ THz is the damping constant; and $\omega_p = \sqrt{Ne^2/\varepsilon_0 m^*}$ is the plasma frequency, with $e = -1.6 \times 10^{-19}$ C, $\varepsilon_0 = 8.854 \times 10^{-12}$ F m^{-1}, and $m^* = 1.3665 \times 10^{-32}$ kg being the electron charge, free-space permittivity, and effective free-carrier mass, respectively. In the temperature range that extends from 160 K to 350 K, the intrinsic career density N (in cm^{-3}) can be found by using the following formula:

$$N = 5.76 \times 10^{14} T^{3/2} \exp(-0.26/2k_B T) \tag{3}$$

where $k_B = 8.62 \times 10^{-5}$ eV K^{-1} is the Boltzmann constant and T is the absolute temperature. Figure 1(b) presents $\mathrm{Re}\,\varepsilon_{\mathrm{InSb}}$ and $\mathrm{Im}\,\varepsilon_{\mathrm{InSb}}$ vs f for several values of T. The transition of InSb from the dielectric state ($\mathrm{Re}\,\varepsilon_{\mathrm{InSb}} > 0$) to the plasmonic state ($\mathrm{Re}\,\varepsilon_{\mathrm{InSb}} < 0$) at a particular frequency occurs at a particular temperature in the range extending from 295 K to 345 K. The frequency at which $\mathrm{Re}\,\varepsilon_{\mathrm{InSb}}$ crosses zero shifts from 2.46 THz at 295 K to 4 THz at 345 K. At a fixed frequency, the applied variation in T can lead to the change $\Delta(\mathrm{Re}\,\varepsilon_{\mathrm{InSb}}) = 40$ in the vicinity of f = 2 THz and the change $\Delta(\mathrm{Re}\,\varepsilon_{\mathrm{InSb}}) = 15$ in the vicinity of f = 3 THz. Hence, a significant difference in TSE may be expected at a fixed frequency as the absolute temperature changes from 295 K to 345 K.

Optics EXPRESS

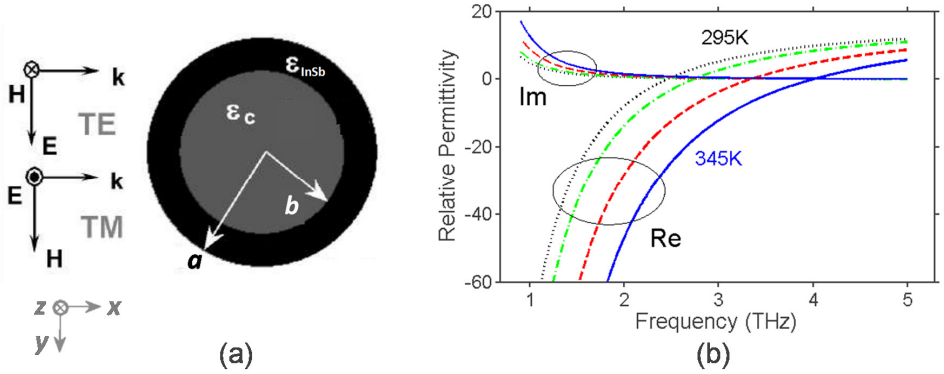

Fig. 1. (a) Geometry of the boundary-value problem. (b) Relative permittivity of InSb at T = 345 K – solid blue lines, (b) 325 K – red dashed lines, 305 K – green dash-dotted lines, and 295 K – dotted black line; Re and Im indicate real and imaginary parts.

3. Effects of temperature for TE-polarized incidence

Let us begin with the analysis of the effects exerted by variations in T on the scattering of an incident TE-polarized plane wave. Figure 2 presents σ as a function of ka when a = 14 μm, $\varepsilon_c = 5$ and either b = 6 μm [Figs. 2(a)-2(d)] or b = 10 μm [Figs. 2(e)-2(h)]. The basic features of these plots include: (i) intermittent minima and maxima of σ, and (ii) weak scattering at some of those minima. These features strongly depend on T.

On comparing Figs. 2(a)-2(d), we observe that the first minimum of σ for b = 6 μm is redshifted from ka = 0.88 to ka = 0.58 when T is decreased from 345 K to 295 K. The second minimum located at ka = 1.2 in Fig. 2(a) is redshifted to ka = 0.74 in Fig. 2(d). The third minimum is redshifted from ka = 1.89 to ka = 1.67, which implies lower sensitivity to the temperature, because ε_{InSb} is then closer to ε_∞ and, therefore, varies less quickly with temperature, as can be observed in Fig. 1(b). One can see that all the features remain in the considered range of temperature, but the magnitudes at the maxima and spectral distances (i.e., Δka) between the consecutive minima of σ are changed together with their locations on the ka axis when T is varied.

The minima of σ correspond to three different ranges of ε_{InSb} variation, i.e., $\mathrm{Re}\,\varepsilon_{InSb} < 0$, $0 < \mathrm{Re}\,\varepsilon_{InSb} < 1$, and $\mathrm{Re}\,\varepsilon_{InSb} > 1$. As shown later, they may arise from different mechanisms of scattering suppression, which all may be possible in one structure. Adjustment of geometric parameters gives one more degree of freedom to control scattering. The main difference between Figs. 2(a)-2(d) and Figs. 2(e)-2(h) is that the deep minima with near-zero σ are not observed for the latter at $ka > 1.5$. The different spectral distances between the consecutive minima for different values of T are also noticeable.

The spectral location of the first minimum depends on b for fixed a, as seen from the comparison of Figs. 2(a)-2(d) and Figs. 2(e)-2(f). At the same time, the spectral location of the second minimum is weakly sensitive to b, so that the effect of the interior region on the scattering could be minimal. In certain conditions, this may enable *masking* of the interior region from a far-zone observer, particularly when the TSE is small. We refer to this phenomenon as *masking of the first type*. The third minimum of σ is present in the vicinity of $ka = 2$. As σ is close to zero for b = 6 μm [Figs. 2(a)-2(d)], but exceeds 0.39 for b = 10 μm [Figs. 2(e)-2(h)] at the third minimum, its usefulness is significantly affected by the thickness of the InSb coating.

We next tried to identify those features of the TSE that arise from each of two components (i.e., core and shell) and those which manifest as their combined effects. In order to quantify possible effects of coating, i.e., *scattering enhancement* and *scattering suppression*, we

Optics EXPRESS

calculated the TSE σ_c for the coated cylinders and the TSE σ_{uc} for the uncoated cylinders. σ_c and σ_{uc} are given by Eq. (1) with $\varepsilon_{\mathrm{InSb}}$ specified by Eq. (2) and with $\varepsilon_{\mathrm{InSb}}$ replaced by 1, respectively. The results of comparison are presented in Fig. 3 in terms of the TSE contrast, $\psi = \sigma_{uc} / \sigma_c$. Scattering suppression due to the coating is indicated by $\psi > 1$, and scattering enhancement due to the coating is indicated by $\psi < 1$. *Ideal invisibility* is the limiting case of scattering suppression that occurs when $\psi \to \infty$. Scattering enhancement is the rather usual effect that can arise due to increases in the electrical size and the volume-averaged relative permittivity by the incorporation of the InSb shell.

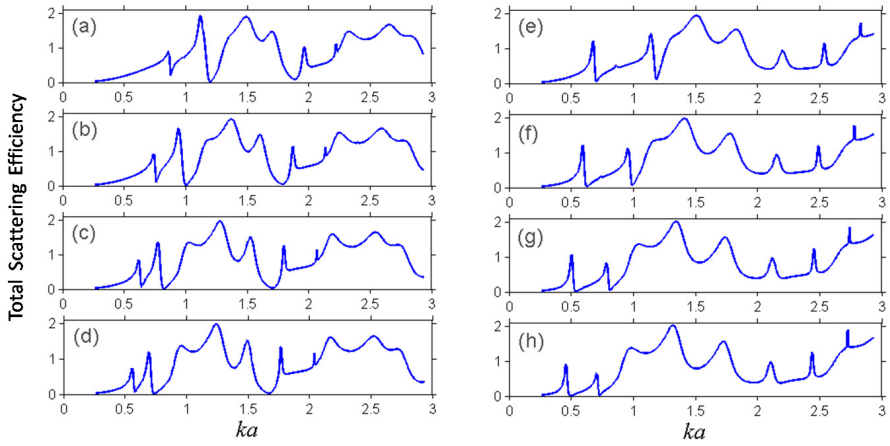

Fig. 2. Total scattering efficiency σ when $\varepsilon_c = 5$ and the incident plane wave is TE polarized; (a-d) b = 6 μm and a = 14 μm, and (e-h) b = 10 μm and a = 14 μm; (a,e) T = 345 K, (b,f) T = 325 K, (c,g) T = 305 K, and (d,h) T = 295 K.

When $\psi = 1$, *masking of the second type* can be obtained when the TSE for both coated and uncoated cylinders significantly deviates from zero, as a far-zone observer cannot recognize the difference between the coated and uncoated cylinders, at least if the data for σ are only available. In contrast with masking of the first type, masking of the second type should appear in the vicinity of but not exactly at some minimum of σ_c, in order to remain in the scattering-suppression regime. Indeed, the minima of σ_c do not coincide with the minima of σ_{uc}, because at least a weak effect of the interior on the depth and location of the minimum of TSE remains. Thus, σ_{uc} may take rather large values at the minima of σ_c that enable $\psi > 1$.

Comparing Figs. 2(a) and 3(a), we conclude that (i) $\psi < 1$ at the first minimum of σ_c and (ii) this minimum does not correspond to a peak of ψ. Let us recall that $\psi < 1$ indicates that scattering by the coated cylinder is stronger than by the uncoated one. In contrast to the first minimum, the second minimum corresponds to a peak of ψ, although $\psi > 1$ is not achieved for all of T-values. In Fig. 3(a), a temperature threshold $T = T_{th}$ exists for the second minimum of σ_c: whereas the InSb shell strengthens scattering for $T < T_{th}$, it suppresses scattering for $T > T_{th}$. Strong suppression can be obtained for the third minimum of σ_c because $\psi > 1$ then for every T between 295 K and 345 K, with higher σ_c achieved for lower T.

Optics EXPRESS

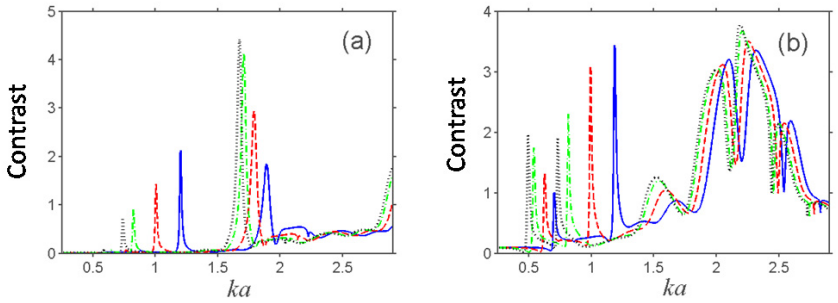

Fig. 3. Contrast $\psi=\sigma_{uc}/\sigma_c$ vs ka for (a) b = 6 μm and (b) b = 10 μm when a = 14 μm, $\varepsilon_c = 5$, and the incident plane wave is TE polarized. Solid blue lines are for T = 345 K, red dashed lines for T = 325 K, green dash-dotted lines for T = 305 K, and dotted black lines for T = 295 K. In order to calculate σ_{uc}, $\varepsilon_{\mathrm{InSb}}$ was replaced by 1.

Both the suppression and enhancement of scattering are strongly sensitive to the choices of a and b. In Fig. 3(b), an example is presented that shows strong scattering suppression at the first and second minima of σ_c when $b = 10\ \mu$m, i.e., for the same parameters as for Figs. 2(e)-2(h). At the first minimum of σ_c, weakening of scattering of cutoff type is obtained while increasing T; thus, $\psi > 1$ can be achieved below the temperature $T = T_c$. At the second minimum of σ_c, the situation is opposite, i.e., scattering is suppressed more as T is increased, similarly to the second minimum of σ_c in Fig. 3(a), but now $\psi > 1$ at the peaks for the whole T-range considered. The trend of variation of $\max\psi$ with T for the third minimum of σ_c in Fig. 3(a) is the same as for the first minimum of σ_c in Fig. 3(b).

Whereas the spectral location of the second minimum is insignificantly affected by b for fixed a, the value of ψ can be strongly sensitive to variations in b. In addition, a wideband increase of the contrast is present in Fig. 3(b) in the neighborhood of ka = 2. However, remains σ_c rather large in this case, see Figs. 2(e)-2(h).

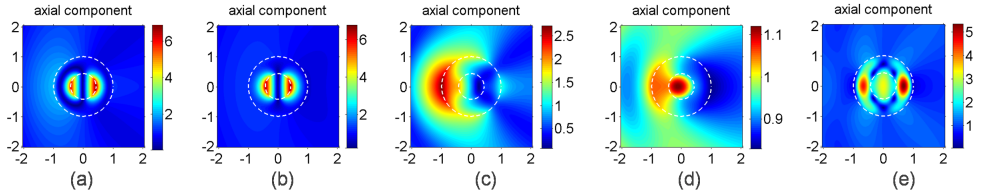

Fig. 4. Spatial profiles of the axial magnetic field when $\varepsilon_c = 5$, b = 6 μm, a = 14 μm, T = 325 K; (a) ka = 0.74 and $\varepsilon_{\mathrm{InSb}} = -11.8 + i0.54$, (b) ka = 0.762 and $\varepsilon_{\mathrm{InSb}} = -10.23 + i0.5$, (c) ka = 0.942 and $\varepsilon_{\mathrm{InSb}} = -1.28 + i0.26$, (d) ka = 1.0 and $\varepsilon_{\mathrm{InSb}} = 0.63 + i0.22$, and (e) ka = 1.79 and $\varepsilon_{\mathrm{InSb}} = 10.98 + i0.0385$. The dashed white lines indicate the core/shell interface. The structure is illuminated by a TE-polarized plane wave propagating from left to right.

To clarify the physics underlying the observed TSE features, Fig. 4 presents the spatial profiles of the axial magnetic field at selected ka-values in Fig. 2(b) for $b = 6\ \mu$m and T = 325 K. They correspond to the first maximum [Fig. 4(a)], first minimum [Fig. 4(b)], second maximum [Fig. 4(c)], second minimum [Fig. 4(d)], and third minimum [Fig. 4(e)] in Fig. 2(b). In Fig. 4(a), two LSPRs are asymmetrically excited on the front and the back segments of the core/shell interface. This asymmetry is expected to be connected with rather large values of the TSE. From the results in Fig. 4(b), it follows that the common effect of the LSPRs that are excited symmetrically on the front and the back segments of the core/shell interface is to weaken scattering. In both cases, higher than a six-fold enhancement of the axial magnetic field occurs in the region in which an LSPR is excited, as compared to the

Optics EXPRESS

incident wave. These results confirm that the first minimum of σ can be connected with the specific field behavior at the core/shell interface, since the spectral location of this minimum is sensitive to variations in b. Indeed, scattering suppression occurs in Fig. 4(b) due to the LSPRs, similarly to the cloaking mechanism of Nicorovici *et al.* [2]. The profile of the electric field in this regime looks like that of a dipole inside an epsilon-negative shell (not shown) [46,47].

Figure 4(c) indicates the excitation of an LSPR on the front segment of the shell/air interface; thus, the role of the interior region is weak. This phenomenon occurs at the second maximum of σ in Fig. 2(b). Again, the asymmetry in LSPR excitation can be correlated to strong scattering. Next, Fig. 4(d) corresponds to the second minimum of σ in Fig. 2(b). Now, the resulting magnetic field is jointly due to a weak LSPR on the shell/air interface and a slightly enhanced magnetic field inside the core. These two effects are expected to compensate each other, the compensation being somewhat similar to scattering cancellation observed in plasmonic cloaking [3,14]. Clearly, values of the TSE for the core alone and the shell alone are significantly larger than the TSE for the core-shell structure, so that a compensation of some kind should appear.

Finally, Fig. 4(e) presents the spatial profiles of the axial magnetic field at the third minimum of σ in Fig. 2(b). The spatial profile indicates the presence of a volumetric resonance with azimuthally inhomogeneous field distribution in the shell that is affected by the core region. The spatial profile is similar to those associated with Fabry–Perot resonances that enable invisibility of high-permittivity shells [4,16], but it looks here rather like that of an azimuthally propagating wave. However, in both Fig. 4(e) and [4], we have a volumetric resonance in a shell separating air from a dielectric material. As $\sqrt{\mathrm{Re}\varepsilon_{\mathrm{InSb}}}k(a-b)\approx 3.4$ in Fig. 4(e), such resonances can appear in the shell; see [4].

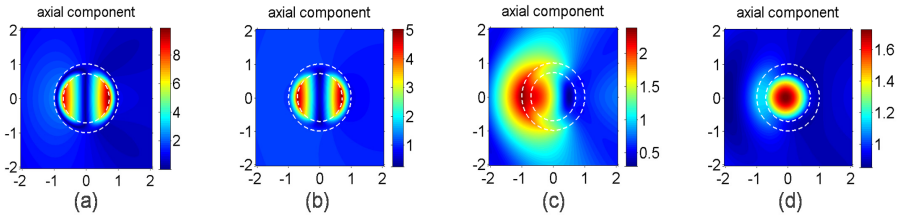

Fig. 5. Spatial profiles of the axial magnetic field when $\varepsilon_c = 5$, b = 10 μm, a = 14 μm, T = 325 K; (a) ka = 0.594 and $\varepsilon_{\mathrm{InSb}} = -26.95 + i1.052$, (b) ka = 0.627 and $\varepsilon_{\mathrm{InSb}} = -22.59 + i0.895$, (c) ka = 0.957 and $\varepsilon_{\mathrm{InSb}} = -0.751 + i0.252$, and (d) ka = 0.992 and $\varepsilon_{\mathrm{InSb}} = 0.388 + i0.226$. The dashed white lines indicate the core/shell interface. The structure is illuminated by a TE-polarized plane wave propagating from left to right.

Figure 5 presents spatial profiles of the axial magnetic field at selected ka-values in Fig. 2(f) for b = 10 μm and T = 325 K. They correspond to the first maximum [Fig. 5(a)], the first minimum [Fig. 5(b)], the second maximum [Fig. 5(c)], and the second minimum [Fig. 5(d)]. The basic features of Figs. 5(a)-5(c) are the same as of Figs. 4(a)-4(c), respectively. Figures 4(d) and 5(d) differ, in particular, in the field-intensity contrast between the LSPR region and the core. There is no analog of Fig. 4(e) for $b = 10\mu$m, because the InSb coating is not thick enough to sustain a volumetric resonance.

We found that all resonances are thermally tunable, so that field maps similar to the ones in Figs. 4 and 5 were obtained for T = 295, 305, and 345 K at the corresponding maxima and minima of the TSE. Hence, there is no need to present field maps at the other three temperatures considered in Fig. 2.

4. Effects of temperature for TM-polarized incidence

Next, we present our results for TM-polarized incidence. Figure 6 contains plots of σ vs ka for the same geometric parameters and temperatures as in Fig. 2. One can see two minima of

Optics EXPRESS

σ in all plots in Fig. 6. The spectral locations of the minima and the spectral distances between two consecutive minima vary with *T*. An increase of *b* leads to some changes in the spectrum of σ but the basic features remain the same, similarly to TE-polarized incidence discussed in Sec. 3. For instance, the first minimum of σ for $b = 6\ \mu$m is redshifted from *ka* = 1.14 to *ka* = 0.716 when *T* is decreased from 345 K to 295 K. Similarly to Figs. 2(a)-2(d), the spectral location of the second deep minimum of σ is less sensitive to the variation of *T*.

The spectral locations of some minima of σ at a fixed temperature are rather weakly sensitive to the polarization state of the incident plane wave, as become clear from comparing Figs. 2(a)-2(d) with Figs. 6(a)-6(d) for $b = 6\ \mu$m. As examples, there are minima at *ka* = 1.2 and *ka* = 0.82 for the TE polarization state and at *ka* = 1.15 and *ka* = 0.8 for the TM polarization state when *T* = 345 K and *T* = 305 K, respectively.

Compared to Fig. 2 for the TE polarization state, the spectral locations of the near-zero minima of σ at fixed temperature depend more strongly on the core radius *b* in Fig. 6 for the TM polarization state. This difference between the two polarization states can be accentuated by a judicious selection of the value of *b*. Clearly, the locations of the minima in Figs. 2(e)-2(h) do not coincide with those in Figs. 6(e)-6(h) for $b = 10\ \mu$m. Hence, spectral regimes of weak scattering with strong and weak sensitivities to the polarization state are available.

Regardless of the mentioned differences, in most of these cases, scattering is quite sensitive to temperature. A relatively weak sensitivity to temperature is observed only for the second minima in Figs. 6(e)-6(h), for which σ is small but not very close to zero.

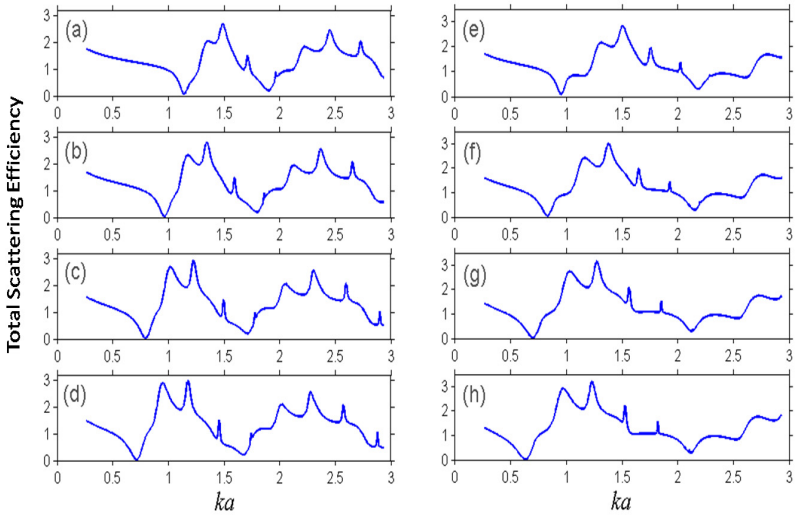

Fig. 6. Total scattering efficiency σ when $\varepsilon_c = 5$ and the incident plane wave is TM polarized; (a-d) *b* = 6 μm and *a* = 14 μm, and (e-h) *b* = 10 μm and *a* = 14 μm; (a,e) *T* = 345 K, (b,f) *T* = 325 K, (c,g) *T* = 305 K, and (d,h) *T* = 295 K.

Figure 7 is the analog of Fig. 3 for TM-polarized incidence. In Fig. 7, $\psi > 1$ at *all* of the considered minima of σ_c; i.e., the InSb shell weakens scattering. For $b = 6$ μm, we obtain $\max\psi \approx 18$ at *T* = 305 K for the first minimum of σ_c, and $\psi > 15$ is achieved also for *T* = 295 K and 325 K in Fig. 7(a). Since the spectral locations of these sharp peaks of ψ change with *T*, *thermally tunable invisibility* is definitely possible. Neither threshold nor cutoff behavior is observed with changing temperature; rather, one can expect an optimal temperature at which ψ is maximal at the peak. The case of $\psi > 1$ is obtained also for the second minimum of σ_c but with only twofold weakening of the TSE.

Optics EXPRESS

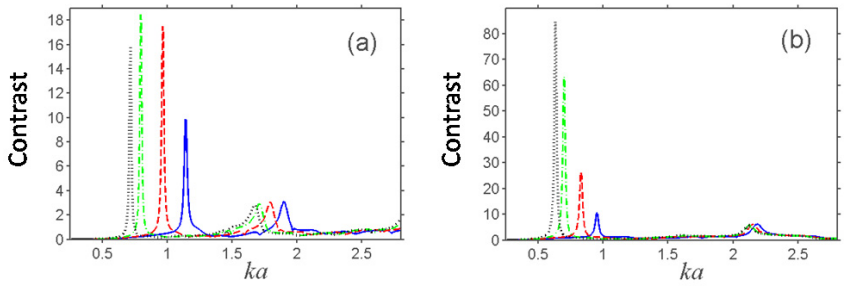

Fig. 7. Contrast $\psi=\sigma_{uc}/\sigma_c$ vs ka for (a) b = 6 μm and (b) b = 10 μm when a = 14 μm, $\varepsilon_c = 5$, and the incident plane wave is TM polarized. Solid blue lines are for T = 345 K, red dashed lines for T = 325 K, green dash-dotted lines for T = 305 K, and dotted black lines for T = 295 K. In order to calculate σ_{uc}, $\varepsilon_{\mathrm{InSb}}$ was replaced by 1.

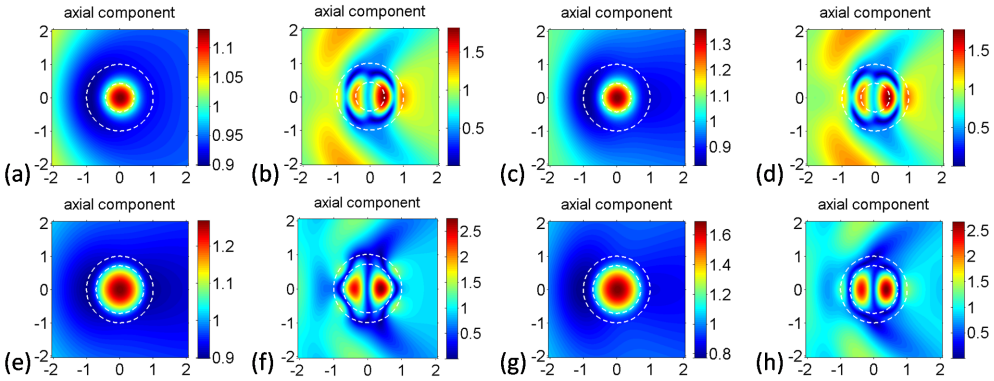

Fig. 8. Spatial profiles of the axial electric field when $\varepsilon_c = 5$, a = 14 μm; (a-d) b = 6 μm; (e-h) b = 10 μm; (a,b,e,f) T = 295 K; (c,d,g,h) T = 325 K; (a) ka = 0.716 and $\varepsilon_{\mathrm{InSb}} = -0.15 + i0.324$, (b) ka = 1.675 and $\varepsilon_{\mathrm{InSb}} = 12.79 + i0.0253$, (c) ka = 0.965 and $\varepsilon_{\mathrm{InSb}} = -0.48 + i0.246$, (d) ka = 1.79 and $\varepsilon_{\mathrm{InSb}} = 10.98 + i0.0385$, (e) ka = 0.63 and $\varepsilon_{\mathrm{InSb}} = -4.76 + i0.476$, (f) ka = 2.12 and $\varepsilon_{\mathrm{InSb}} = 13.87 + i0.0125$, (g) ka = 0.83 and $\varepsilon_{\mathrm{InSb}} = -6.16 + i0.386$, (h) ka = 2.15 and $\varepsilon_{\mathrm{InSb}} = 12.42 + i0.022$. The dashed white lines indicate the core/shell interface. The structure is illuminated by a TM-polarized plane wave propagating from left to right.

When $b = 10\ \mu$m, even stronger suppression of scattering by the InSb coating is available at the first minimum in Fig. 7(b). In this case, $\max\psi > 80$ at T = 295 K, and ψ decreases with increase in T. The core-shell structure is invisible to a far-zone observer at the peak frequencies, for T ranging from 295 K to 345 K. Accordingly, invisibility can be dynamically tuned by changing temperature. As observed in Fig. 7(b) at the second minimum of σ_c, nearly twofold weakening is possible for $b = 10\ \mu$m in Fig. 7(b), just as for $b = 6\ \mu$m in Fig. 7(a). However, due to a weaker effect of T on the spectral location of the minimum, we obtain now a wide range of T, in which ψ can be kept larger than a given value ψ_c, that results from the overlapping of the bell-shaped dependences of ψ on ka for different values of T.

Figure 8 presents examples of the spatial profiles of the axial electric field for $b \in \{6,10\}$ μm and $T \in \{295,325\}$ K. The first minimum of σ is characterized in Figs. 8(a), 8(c), 8(e), and 8(g) by a weak zero-order resonance in a circular resonator (core) with a semi-transparent wall (shell). As shown by a comparison of either Figs. 8(a) and 8(c) or Figs. 8(e) and 8(g), the spatial profiles are the same for two different values of T. Thus, even though the spectral

Optics EXPRESS

location is changed due to a change in the temperature, the underlying mechanism does not change. A strong magnetic field localized to the core/shell interface (not shown) allows one to consider this case also in terms of LSPRs.

At the second minimum, σ remains rather large in Figs. 8(b), 8(d), 8(f), and 8(h), so that it is difficult to unambiguously identify the underlying mechanism. The spatial profiles for $b = 6\ \mu$m and $b = 10\ \mu$m are similar to each other, although the field maximum occurs at the core/shell interface for $b = 6\ \mu$m but inside the core for $b = 10\ \mu$m.

5. Effects of relative permittivity of the core

Let us now consider the effects of ε_c on the TSE. Results are presented for $T \in \{295,345\}$ K and $\varepsilon_c \in \{-450,4,5,11.4,35.4\}$. Figure 9 presents σ as a function of ka when b = 6 μm, a = 14 μm, T = 295 K, for both TE or TM polarization states. From Fig. 9(a) for the TE polarization state, we conclude that the first and the third minima of σ are significantly sensitive to ε_c, but the second minimum is almost unaffected by changes in ε_c; moreover, the second maximum is affected weakly. Qualitatively, these inferences are in good agreement with those drawn from Figs. 2 and 6; hence, the same mechanisms underlie these results as discussed for Figs. 4, 5, and 8. The third minimum of σ is most sensitive to variations in ε_c. For instance, changing ε_c from 5 to 11.4 leads to a redshift from ka = 1.69 to ka = 1.53.

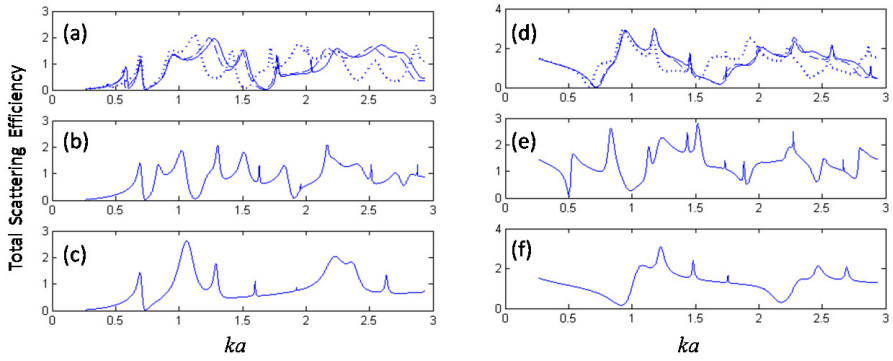

Fig. 9. Total scattering efficiency σ when b = 6 μm, a = 14 μm, T = 295 K, and the incident plane wave is either (a-c) TE polarized or (d-f) TM polarized; (a,d) $\varepsilon_c = 4$ (solid lines), $\varepsilon_c = 5$ (dashed lines), and $\varepsilon_c = 11.4$ (dotted lines); (b,e) $\varepsilon_c = 35.4$; and (c,f) $\varepsilon_c = -450$.

For $\varepsilon_c = 35.4$ in Fig. 9(b), the first minimum disappears, while the second minimum stays at nearly the same spectral location as in Fig. 9(a). The third minimum is redshifted to ka = 1.13, so the difference in the locations of this minimum for $\varepsilon_c = 5$ and $\varepsilon_c = 35.4$ is about $\Delta ka = 0.56$, which corresponds to a redshift of 1.91 THz.

For $\varepsilon_c = -450$ in Fig. 9(c), the minimum being initially the second one remains insensitive to the core material change, so it is useful for masking when the TSE is small. Indeed, as observed in Figs. 9(a)-9(c), the deep minimum of σ in the vicinity of ka = 0.75 is weakly sensitive to ε_c in the considered range of that parameter. Although the core material with $\varepsilon_c = -450$ is purely hypothetical since realistic materials with $\mathrm{Re}\,\varepsilon_c < 0$ are necessarily dispersive, Fig. 9(c) provides insight into the generality of this regime.

For the TM polarization state, the basic features observed in Figs. 9(d)-9(f) are similar to those in Fig. 6. The minima of σ are sensitive to the variations in ε_c. The contrast in σ rather than the shift of the minimum could be used to distinguish between two different materials. For example, there is a high contrast between the cases of high ε_c [Fig. 9(e)] and

Optics EXPRESS

low ε_c [Fig. 9(d)] in the vicinities of ka = 0.5 and ka = 1, so that a high-permittivity core material can be distinguished from a low-permittivity one.

Clearly, the weak dependence of σ on ε_c at ka = 1 in Fig. 9(d), which can be used for masking at large TSE, is connected with the fact that the scattering is mainly determined by the shell/air interface for $\varepsilon_c \in \{4,5,11.4\}$; but the same is not true for $\varepsilon_c = 35.4$ in Fig. 9(e). Similarly to the case of $\varepsilon_c = 35.4$, scattering is weakened in Fig. 9(f) in the vicinity of ka = 1 by the incorporation of the InSb shell for $\varepsilon_c = -450$. However, there is no minimum near ka = 0.5 in this case, so that high-permittivity and negative-permittivity core materials can be distinguished from each other.

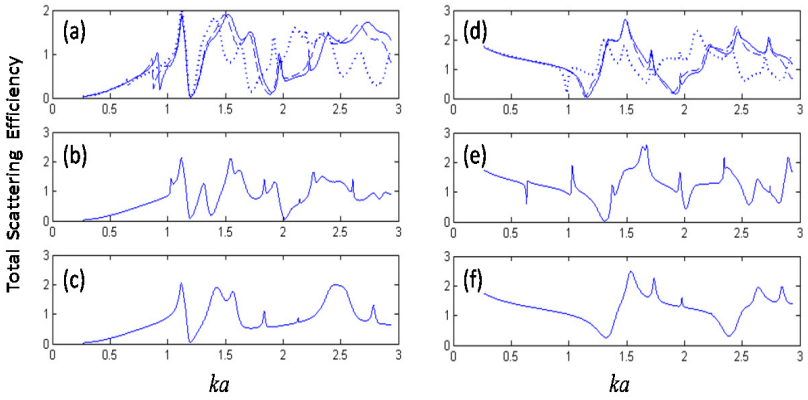

Fig. 10. Total scattering efficiency σ when b = 6 μm, a = 14 μm, T = 345 K, and the incident plane wave is either (a-c) TE polarized or (d-f) TM polarized; (a,d) $\varepsilon_c = 4$ (solid lines), $\varepsilon_c = 5$ (dashed lines), and $\varepsilon_c = 11.4$ (dotted lines); (b,e) $\varepsilon_c = 35.4$; and (c,f) $\varepsilon_c = -450$.

A temperature increase typically results in blueshifts of all minima. This is exemplified by a comparison of Fig. 9 for T = 295 K with Fig. 10 for T = 345 K, all parameters other than the temperature being the same for the two figures. The spectral distances between consecutive minima of σ (near zero) can decrease on temperature increase, as happens with (i) $\varepsilon_c = 35.4$ for the TE polarization state in Figs. 9(b) and 10(b) as also with (ii) $\varepsilon_c = 5$ and $\varepsilon_c = 11.4$ for the TM polarization state in Figs. 9(d) and 10(d). The minimum of σ, which is weakly sensitive to ε_c, is located now in the vicinity of ka = 1.2 (TE polarization state). The difference in the spectral locations of the first deep minimum of σ for high-permittivity and negative-permittivity core materials for the TM polarization state in Figs. 10(e) and 10(f) is insignificant.

Examples of the spatial profiles of the axial magnetic field for the TE polarization state are presented in Fig. 11. In Figs. 11(a)-11(d), the selected ka-values correspond to the third minimum of σ for $\varepsilon_c = 11.4$, whereas it is blueshifted for $\varepsilon_c = 4$ and 5. The main difference between weak scattering for $\varepsilon_c = 11.4$ [Figs. 11(b) and 11(d)] and strong scattering for $\varepsilon_c = 5$ [Figs. 11(a) and 11(c)] is the field resonance in both the core and the shell regions in the former case, while it occurs only in the shell in the latter case. A comparison of Figs. 11(a) and 11(c) and Figs. 11(b) and 11(d) shows that a very similar field distribution can be obtained while staying at the corresponding minimum that is redshifted/blueshifted on changing the temperature.

Optics EXPRESS

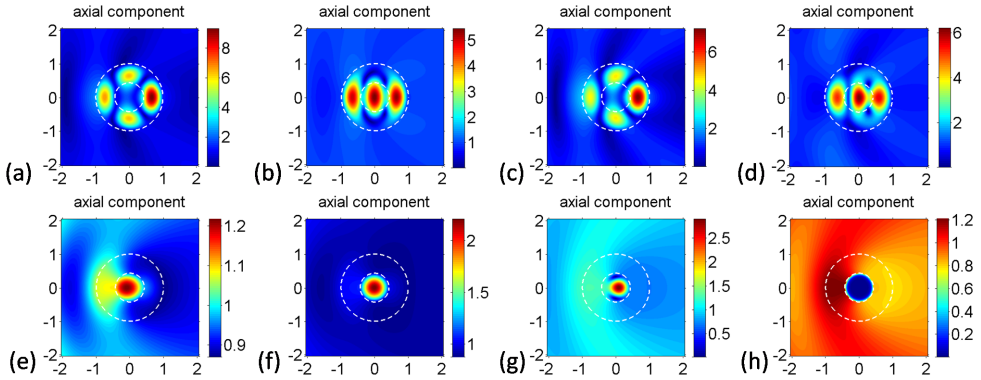

Fig. 11. Spatial profiles of the axial magnetic field when b = 6 μm, a = 14 μm; (a,b) ka = 1.53, T = 295 K and $\varepsilon_{\mathrm{InSb}} = 12.2 + i0.033$; (c,d) ka = 1.73, T = 345 K and $\varepsilon_{\mathrm{InSb}} = 8.48 + i0.061$; (e-h) ka = 1.2, T = 345 K and $\varepsilon_{\mathrm{InSb}} = 0.72 + i0.183$; (a,c,e) $\varepsilon_c = 5$; (b,d,f) $\varepsilon_c = 11.4$; (g) $\varepsilon_c = 35.4$; and (h) $\varepsilon_c = -450$. The dashed white lines indicate the core/shell interface. The structure is illuminated by a TE-polarized plane wave propagating from left to right.

Next, Figs. 11(e)-11(h) show the spatial profile of the axial magnetic field at the second minimum of σ in Figs. 10(a)-10(c). Its spectral location is weakly sensitive to variations in ε_c. The LSPR at the shell/air interface and the field enhancement inside the core are expected to compensate for each other. Although somewhat differently for different values of ε_c, a general feature is that the field is rather weak inside the shell but enhanced in the core region, as can be seen in Figs. 11(e)-11(g).

The TSE is near zero for $\varepsilon_c = -450$, i.e., when the field is vanishingly small inside the core. Hence, the resulting mechanism to weaken scattering can differ from the aforementioned compensation one, because the weak or vestigial LSPR is enough to obtain a small value of σ, while the field in the core at $\varepsilon_c > 1$ can be weakly coupled to the exterior. Therefore, a more detailed study of the mechanism leading to weak dependence of σ to ε_c will soon be undertaken.

6. Concluding remarks

We theoretically examined the thermal tunability of the total scattering efficiency of an infinitely long dielectric cylinder coated by InSb and illuminated by a linearly polarized plane wave whose electric or magnetic field (but not both) is aligned parallel to the cylinder axis. InSb is a thermally tunable semiconductor showing transition from the dielectric state to the plasmonic state at THz frequencies when the temperature is increased.

For TE-polarized incidence, the first and second minima of the total scattering efficiency can be redshifted by more than 30% in the frequency domain by a 50-K decrease in temperature, when the relative permittivity of core material equals 5. Weakening of scattering at the first minimum for the coated cylinder is typically connected with the excitation of a localized surface-plasmon resonance at the core/shell interface. The electric field appears similar in spatial profile to that of an electric dipole inside a negative-permittivity shell. The second minimum can be associated with compensation of the effects of the different parts of the entire structure, or even with the simultaneous disappearance of these effects. The third minimum of the TSE (that may appear when thickness of the InSb coating is large enough) can be associated with a volumetric resonance in the shell.

For TM-polarized incidence, the first minimum of the TSE is redshifted by more than 35% with a 50-K decrease in temperature for the same core material. This minimum corresponds to the axial electric field that represents a weak zero-order resonance in a circular resonator (core) with a semi-transparent wall (coating). On the other hand, a strong magnetic field localized to the core/shell interface allows to consider this case also in terms of LSPR.

Optics EXPRESS

The TSE usually remains rather large at the second minimum, making it difficult to unambiguously identify the underlying mechanism. All of the aforementioned minima are preserved but spectrally shifted when the absolute temperature varies between 295 K and 345 K. The locations of the minima and the spectral distances between consecutive minima appear useful for temperature sensing.

Scattering can be suppressed by the incorporation of the InSb coating. This effect is especially strong for the TM polarization state, leading to more than 80-fold weakening of the scattering compared to the corresponding uncoated core. Hence, thermally tunable invisibility can be realized at THz frequencies. Weakening of scattering may appear either over narrow or broad ranges of temperature. Besides, the coated and the uncoated cylinders can have the same TSE at specific frequencies and temperatures, so that a far-zone observer cannot distinguish between them. In other words, the core can be masked by the InSb shell. Comparison of the results obtained for different core materials indicates the existence of the scattering regimes, which are either weakly or significantly sensitive to the variations in core's relative permittivity. Weak-sensitivity regimes can be exploited to mask the core from a far-zone observer. Strong-sensitivity regimes will allow one to distinguish between materials with significantly different relative permittivity.

The basic scattering features and their sensitivity to temperature endure for a wide variety of core materials, including high-permittivity and negative-permittivity materials. Hence, efficient strategies to achieve tunable invisibility and masking can be developed. Some of the reported effects and regimes can be obtained even for thinner InSb coatings, e.g., for $b = 13\ \mu\text{m}$. Our conclusions are not restricted to the use of InSb but should hold for coatings of other thermally sensitive materials as well. Furthermore, extensions to metamaterials comprising arrays of thermally tunable cylinders should be possible. Effects of phase as well as those of bright and dark LSPRs are planned for future studies in the context of the discussed scattering scenarios. The richness of the palette of achievable effects is promising for multifunctionality, i.e., when either two functions are combined in one spectral regime, or different functions are realized in different spectral regimes, in one device [48–50].

Funding

Narodowe Centrum Nauki (NCN), Poland (MetaSel DEC-2015/17/B/ST3/00118); DPT (HAMIT); TUBITAK (113E331, 114E374, 115F560).

Acknowledgments

E.O. acknowledges partial support from the Turkish Academy of Sciences. A.L. thanks the Charles Godfrey Binder Endowment at the Pennsylvania State University for ongoing support of his research activities.